132 (2024) 205486

Contents lists available at ScienceDirect

Gas Science and Engineering

journal homepage: www.journals.elsevier.com/gas-science-and-engineering

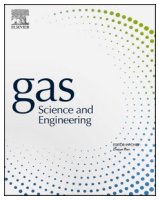

Evaluation of CO_2 leakage potential through fault instability in CO_2 geological sequestration by coupled THMC modelling

Lian Chen [a,b], Derek Elsworth [c], Jianye Chen [d], Quan Gan [a,b,*]

[a] School of Resources and Safety Engineering, Chongqing University, Chongqing, China
[b] State Key Laboratory of Coal Mine Disaster Dynamics and Control, Chongqing, China
[c] Department of Energy and Mineral Engineering, EMS Energy Institute and G3 Center, Pennsylvania State University, University Park, PA, USA
[d] State Key Laboratory of Earthquake Dynamics, Institute of Geology, China Earthquake Administration, Beijing, China

ARTICLE INFO

Keywords:
THMC coupling
CO_2 sequestration
Fault stability
Mineral transport
Porosity and permeability

ABSTRACT

A faulted saline aquifer system was simulated in a coupled thermal-hydraulic-mechanical-chemical (THMC) framework to examine the potential breaching of the caprock seal from long-term CO_2 sequestration. The pH of the brines steadily dropped from 7.5 to 4.7 due to the continuous injection of $scCO_2$ (supercritical CO_2), which was caused by the rapid dissolution of calcite in the reservoir and associated fault zones, alongside alterations in the concentrations of primary and secondary minerals within the formation. The increase in pore pressure with the continuous injection of $scCO_2$ triggered fault reactivation at 6y with the resultant leakage of CO_2 along the fault. This builds CO_2 saturation inside the fault at 7y to six-fold higher than pre-slip. Continuing shear reactivation and creation of reactive surface area following the initial CO_2 leakage accelerates dissolution/precipitation reactions, in turn further increasing porosity and permeability of the reservoir and fault. In particular, the permeability and porosity in the fault zone were increased by only 2% and 6%, respectively – staunched by competitive feedbacks in dissolution countered by precipitation that are individually much larger. Comparison of mineral concentrations adjacent to the fault before-and-after instability revealed that the development of shear failure also promotes the transport of reactivated minerals into the fault zone. Among them, feldspar changes most significantly in later stages, dominated by dissolution with the volume fraction decreasing by 80% and increasing the aqueous concentration of K^+ by approximately an order of magnitude. However, secondary minerals counter this dissolution through precipitation with the volume fraction of kaolinite increasing by an order of magnitude compared with the original fraction. Finally, the evolution of the fault sealing coefficient (F_S) demonstrates that the porosity and permeability exert a pivotal influence in controlling the self-sealing behavior in the basal of the fault, while the upper fault layer exhibits self-enhancing response. A notable observation is that changes in mineral ion concentrations in fault zones could be applied as a significant diagnostic signal to monitor fault stability and the potential for progress of self-sealing behavior.

1. Introduction

Utilizing saline aquifers for carbon capture and storage (CCS) offers a thoroughly validated and well-established strategy to alleviate the release of anthropogenic greenhouse gases into the atmosphere (Reddy et al., 2022). Several pilot projects conducted globally have successfully demonstrated the safety and reliability of the CCS technique. In this, supercritical CO_2 is injected into the deep subsurface and may remain physically or chemically trapped over geological time scales (Alexey et al., 2022; Shi et al., 2022). The target reservoir can effectively retain the injected CO_2 for a minimum duration of 1000 years, as supported by theoretical and modeling investigations. Studies based on theory and modeling have shown that injected CO_2 has the potential to stay within the intended reservoir for a minimum of 1000 years (Wang et al., 2022). However, the injection of significant quantities of CO_2 into aquifers and reservoirs initiates various interconnected thermal-hydraulic-mechanical-chemical (THMC) processes. These processes involve heat transfer, the flow of multiple fluid phases, geomechanical reactions (like strain and stress), and geochemical interactions between the injected fluid and the minerals present in the formation (Yin et al., 2011).

However, injecting excessive volumes of CO_2 into saline aquifers may also result in potential geohazards from the elevated fluid

* Corresponding author. School of Resources and Safety Engineering, Chongqing University, Chongqing, China.
E-mail address: quan.gan@cqu.edu.cn (Q. Gan).

https://doi.org/10.1016/j.jgsce.2024.205486
Received 20 April 2024; Received in revised form 3 November 2024; Accepted 6 November 2024
Available online 6 November 2024

pressures. Among these are potential issues such as the degradation of caprock mechanical integrity and fault reactivation, both of which could lead to the leakage of injected CO_2. (Valentina et al., 1999; Ellsworth and William, 2013; Nicol et al., 2011; Shemeta et al., 2012; Suckale, 2010). Various investigations, ranging from laboratory experiments to field-scale studies, have been conducted to comprehend the interconnected processes associated with breaching caprock sealing (Taghizadeh et al., 2019; Yoosook and Maneeintr, 2018; Andersen et al., 2017). In addition, the vast majority of suitable reservoirs aquifers are surrounded by a limited number of low-permeability faults (González-Nicolás et al., 2019). The injection of massive amounts of CO_2 will pressurize the target sequestration zone and lead the CO_2 plume to propagate over hundreds of kilometers over several decades (Cerasi et al., 2018). Pre-existing faults that penetrate and transect the caprock may be reactivated during CO_2 injection due to an elevation in shear stress applied to the fault plane (Espinoza et al., 2018; Schwab et al., 2017).

Thermo-hydro-mechanical-chemical (THMC) interactions also influence the security of CO_2 geological sequestration through the geochemical influence on the evolution of rock properties and thus fluid pathways (Zhang et al., 2015). Permeability stands out as a pivotal parameter governing the rate of CO_2 leakage, primarily influenced by initial mechanical compaction and deformation stages (Jing et al., 2019). However, the analysis of creep strains suggests that the CO_2-brine-rock reaction plays a substantial role in sealing mechanisms, primarily due to the generation of carbonic acid (Zhou et al., 2018). Mineral precipitation and dissolution represent the main geochemical mechanisms that impact permeability evolution, usually becoming more pronounced at later stages and with lesser intensity (McDermott et al., 2015; Lang et al., 2015; Yasuhara et al., 2016; Ogata et al., 2018). The presence of clay particles, released through the dissolution of carbonate cements, can significantly contribute to mineral precipitation processes that result in a reduction of fracture permeability by up to five orders of magnitude (Caulk et al., 2016). These clay particles are transported within the fluid and tend to accumulate in pore throats (Yu et al., 2012; Yasuhara et al., 2016; Ma et al., 2017). Pronounced mineral dissolution and precipitation can alter the CO_2 flow path and storage capacity in porous media (Rohmer et al., 2016). An increase in mineral precipitation in the reservoir will reduce feasible CO_2 injection rates (Pruess and Muller, 2009). When the predominant reaction in the caprock is dominated by precipitation, it may reduce CO_2 intrusion into the caprock and improve the caprock seal (Li et al., 2022). Among them, the precipitation of clay minerals such as kaolinite and quartz can lead to a decrease in both the porosity and permeability of the caprock, which helps mitigate the risk of CO_2 leakage (Andreani et al., 2008). But the active dissolution of minerals can result in mechanical degradation, leading to a decrease in strength and an elevated risk of caprock failure (Perera et al., 2016; Falcon-Suarez et al., 2017; Guglielmi et al., 2017). Faults as pre-disposed weak and conductive pathways, may be reactivated in their complex tectonic structure, potentially resulting in the creation of a permeable pathway and fugitive emissions to the surface (Minh and Birendra, 2021; Saro and Birendra, 2021). The migration of CO_2-enriched fluids through faults or fractures carries the potential to initiate water-rock reactions, thereby potentially modifying the fluid transmission properties of the fault. The combined impacts of pressure solution, mineral dissolution/precipitation and temperature change may all conspire to cause changes in porosity, impact capillary diameters and hydraulic apertures and thus change pore and fracture permeabilities. In addition, faults may undergo either “self-sealing” through mineral precipitation or “self-enhancing” via mineral dissolution. (Patil et al., 2017).Therefore, acquiring a profound understanding of the intricate interplay of coupled THMC processes and the resultant CO_2-induced modifications in the fluid flow dynamics of formations is of utmost importance.

To this end, the dynamic evolution of CO_2 distribution in a faulted saline aquifer subjected to geomechanical and geochemical reactions is analyzed using a fully-coupled THMC model (FLAC3D-TOUGHREACT). This numerical model allows for the simultaneous solution of heat transfer, fluid flow, plastic deformation and reactive chemical transport response, together with complex spatiotemporal feedbacks amongst these, in contributing to the evolving porosity and permeability of the system. The ultimate goal is to develop a linkage between changes in mineral contents and attendant permeability on and around, by examining the degree of mineral dissolution and precipitation following CO_2 leakage caused by fault reactivation, in relation to fault porosity and sealing. This involves monitoring the change of mineral ion concentration in fault zone and to define the attendant likelihood for CO_2 leakage through fault failure processes during sequestration.

2. Theoretical model

A coupled model is employed to capture the conservation of mass for fluids and species, as well as mineral transformations governed by permeability changes induced by fault reactivation, while simultaneously determining the timing of fault activation through an analysis of stress evolution. And the assumptions about the developed model can be summarized as follows.

(a) The flow of CO_2 within the permeable medium is governed by the Darcy’s law and mass conservation.
(b) The CO_2-rock interaction does not affect the rock’s modulus and strength, but it facilitates changes in porosity and permeability.
(c) The structure of fault damage zones is comprised of ubiquitous joints, and permeability is defined through the apertures of three sets of orthogonal fractures.
(d) CO_2 is injected into the fully saturated saline aquifer, while without considering the heterogeneity of pore structure in the reservoir formations.

2.1. Mass conservation

The TOUGHREACT-FLAC3D implementation is employed to capture the intricate interplay of THMC coupling phenomena inherent in fluid injection into a CO_2 geological storage reservoir (Gan et al., 2015), which has been extensively used to solve the problem of geological fault instability (Gan and Elsworth, 2014a, 2014b). Mass conservation for flow through permeable media is defined as (Pruess, 2004):

$$\frac{d}{dt}\int_{Vn} M dV_n = \int_{\Gamma_n} F.n d\Gamma_n + \int_{Vn} q dV_n \tag{1}$$

Where the integral describes the flow system over any region V_n, defined by the closed surface Γ_n. Equation (1) signifies that the accumulation of mass within V_n equals the balance between the net inflow of mass across its outer boundary and the outflow from the volume itself. In the cumulative expression, the variable M signifies the mass density of the fluid. F denotes the mass flux, while q represents the mass rate sink/source term. n demonstrates a normal vector pointing out from V_n on the external contour $d\Gamma_n$.

2.2. Mechanical equilibrium

The mechanical equilibrium of the system is established through the equilibrium of momentum as,

$$\sigma_{ij,j} + f_i = p\frac{dv_i}{d_t} \tag{2}$$

The stress tensor component σ_{ij} and the body force component f_i are involved, while the velocity of solid particles is denoted as v_i. When self-weight is considered and inertial effects are disregarded, the formula for the balance equation is presented in equation (3) (Wu et al., 2010),

$$\sigma_{ij,j} + f_i = 0 \tag{3}$$

Incorporating thermal expansion effects, the constitutive relation for the deformable porous medium is established by the poroelastic response (1 and 2 represent the fracture and matrix, respectively) as follows:

$$\sigma_{ij} = 2G\varepsilon_{ij} + \frac{2G\nu_i}{1-2\nu}\varepsilon_{kk}\delta_{ij} - \left(\alpha_p^1 p + \alpha_p^2 p\right)\delta_{ij} - \alpha_T T\delta_{ij} \tag{4}$$

The definition of the stress-strain relation is as follows: Shear modulus (G), rock temperature (T), fluid pressure (p), Poisson ratio (ν), Biot coefficient (α), and thermal expansion coefficient (αT) are all represented by the letters (Zhang et al., 2018),

$$\varepsilon_{ij} = \frac{1}{2}\left(\mu_{i,j} + \mu_{j,i}\right) \tag{5}$$

The Navier-type equation is obtained by combining equations (2)–(5) (Zhang et al., 2019):

$$G\nabla\mu_{i,kk} + \frac{G}{1-2\nu}\mu_{k,ki} - \left(\alpha_p^1 p + \alpha_p^2 p\right)_{,i} - \alpha_T T_{,i} + f_i = 0 \tag{6}$$

2.3. Kinetic mineral dissolution/precipitation

The Arrhenius equation (Lasaga, 1984; Steefel and Lasaga, 1994) offers a reasonable approximation for the temperature dependency of the reaction rate constant. Given that numerous rate constants are documented at 25 °C, it becomes convenient to portray their temperature dependence through a temperature-based function as,

$$\mathrm{k} = k_{25}\exp\left[\frac{-E_a}{R}\left(\frac{1}{T} - \frac{1}{298.15}\right)\right] \tag{7}$$

Here, E_a represents the activation energy, k_{25} stands for the rate constant at 25 °C, R denotes the gas constant, and T represents the absolute temperature. H^+ (acid mechanism) and OH^- (base mechanism) frequently act as catalysts in the dissolution and precipitation of minerals. In the kinetic rate constant k for numerous minerals, each of these three mechanisms is typically considered (Palandri and Kharaka, 2004),

$$\mathrm{k} = k_{25}^{nu}\exp\left[\frac{-E_a^{nu}}{R}\left(\frac{1}{T} - \frac{1}{298.15}\right)\right] + k_{25}^{H}\exp\left[\frac{-E_a^{H}}{R}\left(\frac{1}{T} - \frac{1}{298.15}\right)\right]a_H^{nH} + k_{25}^{OH}\exp\left[\frac{-E_a^{OH}}{R}\left(\frac{1}{T} - \frac{1}{298.15}\right)\right]a_H^{nOH} \tag{8}$$

The superscripts or subscripts nu, H, and OH denote the neutral, acid, and base mechanisms, respectively. a represents the activity of the species, while n denotes a constant power term.

2.4. Porosity and permeability changes

In a dual-porosity medium, the development of permeability and porosity is governed by constitutive relationships, which account for the stress-dependent changes in permeability and the occurrence of mineral dissolution/precipitation as (Davies J.P & Davies D.K, 2001; Rutqvist et al., 2002),

$$\varphi = \varphi_r + (\varphi_0 - \varphi_r)e^{-\alpha\tau'} \tag{9}$$

φ_0 represents the initial porosity under zero effective stress, while φr signifies the porosity under increased effective stress conditions. The effective mean stress, τ', and α, a constant denoting rock compressibility (measured in 1/Pa), are fundamental components of the system. Alterations in mineral mass within the continuum exert a direct influence on the porosity of both fractures and matrix elements. These changes are, in turn, influenced by variations in the overall volume fraction (Peter and Lichtner, 1996):

$$\varphi_c = 1 - \sum_{m=1}^{N_m} f_m - f_u \tag{10}$$

In the iterative modeling process, N_m, representing the total number of reactive minerals, is considered. The total mineral volume fraction ($V_{mineral}/V_{medium}$) for the m-th mineral is also examined, denoted as f_m, while f_u denotes the fraction of nonreactive minerals. The process quantifies how dissolution/precipitation affects porosity by calculating the relative volume fraction change ($\Delta_{\varphi c}$) concerning the initial total volume fraction:

$$\Delta\varphi_c = \varphi_c - V_{ini-m}/V_{medium} \tag{11}$$

$$\varphi_{total} = \varphi + \Delta\varphi_c \tag{12}$$

The evolution of fracture aperture, influenced by the effective normal stress state (σ') acting on the fracture plane, undergoes changes as normal closure and shear reactivation occur on fractures u_{js}. This leads to an increase in the normal aperture b_{dila} through dilation (Taron et al., 2009),

$$b_s = b_r + (b_{\max} - b_r)\exp\left(-\eta\left(\sigma' - \sigma_0'\right)\right) \tag{13}$$

$$b_{dila} = u_p \tan\psi_d \tag{14}$$

where the residual aperture b_r (m) indicates determined experimentally, and the maximum aperture $b_{\max}$ (m) represednts evaluated when the fracture is at zero stress state, the non-linear fracture stiffness η expressed as 1/MPa, the plastic shear strain increment u_p, and the dilation angle ψ_d.

In the parallel-plate mode, the fractures exhibit permeability (Snow and David, 1969) can be determined using a final composite expression that accounts for the cubic relationship between fracture aperture and fracture spacing s:

$$k = \frac{b_{total}^2}{12s} \tag{15}$$

2.5. Fault stress state analysis

The potential for fault reactivation due to fluid pressurization is evaluated from the effective stress,

$$\sigma' = \sigma_n - p \tag{16}$$

where σ_n' represents the effective positive stress, σ_n denotes the total positive stress, and P signifies the pore pressure. The stability of faults is defined using the Mohr-Coulomb failure criterion and the effective stress law as (Jaeger and Cook, 1979; Li et al., 2020),

$$\tau_r = c + \mu_s\sigma_n' \tag{17}$$

τ_r, defined as the critical shear stress, is determined alongside c, representing the cohesive force, and μ_s, which stands for the friction coefficient,

$$\mu_s = \tan\varphi \tag{18}$$

The friction angle, φ, is a defining factor. The shear stress, τ, and the normal stress, σ_n', applied on a preexisting fault plane can be described in terms of the two-dimensional plane principal stresses as,

$$\sigma_n' = \frac{\sigma_1 + \sigma_3}{2} + \frac{\sigma_1 - \sigma_3}{2}\cos 2\theta - \tau_{xz}\sin 2\theta - p \tag{19}$$

$$\tau = \frac{\sigma_3 - \sigma_1}{2}\sin 2\theta + \tau_{xz}\cos 2\theta \tag{20}$$

Once the critical shear stress τ_r is reached, fault slip ensues, and assessing fault stability entails determining the Coulomb stress ratio ω. This ratio is defined as the shear stress divided by the effective normal stress (Ma

et al., 2024),

$$\omega = \frac{\tau}{\sigma_n'} \tag{21}$$

At last, the THMC coupling processes can be summarized as follows: As detailed in equation (3), poroelastic effects drive the interaction among mechanical, hydraulic, and thermal processes. The changes in porosity and permeability resulting from these effects are crucial in influencing the system's behavior, as illustrated by equations (9) and (10). Convective heat transfer (equation (7)) links hydraulic and thermal processes, while temperature-induced changes in fluid properties, including viscosity and density, are outlined in equations (8) and (12). Chemical processes interact with other systems in three main ways: (i) advective transport facilitates the exchange between chemical and hydraulic processes (equation (1)), with fluid density changes managed by equation (12); (ii) changes in porosity and permeability due to mineral dissolution and precipitation, impacting mechanical behavior, as shown by equations (9) and (11), these effects are not simply geometrically added but are combined through a complex multiphysics coupling approach, where chemical and mechanical deformations iteratively influence each other's impact on porosity and permeability, ensuring that the interactions reflect the evolving nature of the system. And (iii) temperature-sensitive chemical reactions, governed by the Arrhenius equation (7), highlight the close relationship between chemical activity and thermal changes.

3. Model set-up

The THMC computational platform, TOUGHREACT-FLAC3D (Taron and Elsworth, 2009), is employed for numerical simulations. This platform, which has been widely validated, calibrated, and applied, is particularly effective in addressing reservoir geomechanics issues, such as induced fault instability (Rinaldi et al., 2016; Gan et al., 2014a, 2014b). Within the proposed numerical model, a conceptual pseudo 3-D geometry is embraced, delineated by a vertical profile with dimensions measuring 4000 m × 10 m × 3500 m. It incorporates a fault zone that intersects a reservoir layer with a thickness of 50 m, which is bounded by two low permeability sealing strata-a caprock and underseal, each with a thickness of 200 m. The steeply dipping fault zone is located centrally between the left and right lateral boundaries of the model and dips an angle of 80° (Fig. 1). The $scCO_2$ injection is approximately 1200m from the fault, at mid-height within the reservoir and at a constant injection rate of 0.1 kg s^{-1} for 7y, and the ppm of the formation water is 5844. The initial formation temperature of this system is 80 °C, with a pressure gradient of 9.8 MPa km^{-1}. A value of 28° is assigned as the internal friction angle of the fault.

Table 1 provides information about the rock and fault properties, while Tables 2–3 provides the corresponding kinetic parameters for all minerals (Gan et al., 2021). While Gan et al. primarily concentrate on the influence of mineralogical geochemical reactions on geothermal energy extraction, this study predominantly focuses on investigating alterations in fault stability within the framework of CO_2 geological storage.

4. Results

Continuously injected $scCO_2$ will exist in the porous medium or be dissolved in water as microscopic residual gas, lowering the pH of the formation fluid. Furthermore, it has the ability to be absorbed by the formation's primary minerals, starting a chain of chemical reactions that lead to the creation of secondary minerals. These reactions result in the formation of carbonate, which is effectively sealed within the geological formation. Moreover, through the interaction of dynamic processes, the reservoir undergoes temporal and spatial evolution, leading to changes in both porosity and permeability.

4.1. CO_2 dissolution

$scCO_2$ is injected into the reservoir, resulting in the formation of three distinct regions: a zone characterized by a high concentration of CO_2, an area where CO_2 and water undergo two-phase mixing, and a region comprising pure water. The equilibrium between the gaseous and aqueous phases of CO_2 is maintained within these regions as follows:

$$CO_2(sc) \rightleftharpoons CO_2(aq);\ CO_2(aq) + H_2O \rightarrow HCO_3^- + H^+ \tag{22}$$

The aqueous phase is referred to as "aq" and the supercritical state as "sc". The reaction that is being described shows that the dissolving of CO_2 causes the brine to become more acidic due to the production of carbonic acid, which aids in solubility capture. Because of the initial high porosity and permeability, the brine-CO_2 mixture is largely transported within the reservoir and cannot escape into the confining layers.

Fig. 2 shows the distributions of water-soluble CO_2 mass fraction from 1y to 7y, and the distribution of pH evolved at 3y and 7y respectively. The extent of the acidified brine with dissolved CO_2 gradually expands with the continued injection of $scCO_2$, and migrates to the fault at 3y (Fig. 2 (b)). The pH of the reservoir fluids falls from 7.5 to 5.7 after 1y, finally dropping to 4.7 after 7y (Fig. 2 (f)). The pH of the water within the fault changes until the water-soluble CO_2 gradually diffuses into the center of the fault zone (Fig. 2 (e)) after 3y, resulting in a decrease in pH from 6.5 to 4.7 (Fig. 2(e) and (f)). This indicates that the aqueous solution is increasingly more corrosive and may result in hydrogeochemical interactions with varying intensities in the formation. In addition, the aqueous CO_2 has penetrated into the center of the fault core (Fig. 2 (d)), thus it is inferred that the continuous shear failure of the activated fault after 5y resulted in CO_2 penetrating the fault at 7y.

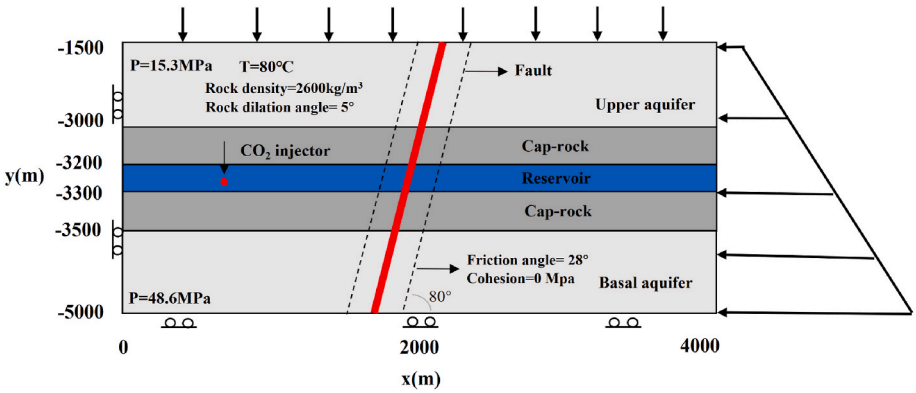

Fig. 1. Illustration of conceptual model and dimensions including the aquifer, caprock and fault.

Table 1
Assigned mechanical and hydraulic properties of the domains indicated in Fig. 1.

	Reservoir	Caprock	Upper Aquifer	Basal Aquifer	Damage Zone	Fault core
Porosity, φ	0.3	0.01	0.1	0.01	0.1	0.1
Permeability, (k, m^2)	1×10^{-13}	1×10^{-19}	1×10^{-14}	1×10^{-18}	1×10^{-15}	1×10^{-17}
Res. porosity, φ_{res}	2.95×10^{-2}	0.5×10^{-3}	0.95×10^{-2}	0.5×10^{-3}	0.95×10^{-2}	0.95×10^{-2}
Rock density, ρ (kg/m^3)	2600	2600	2600	2600	2600	2600
Young's modulus, E (GPa)	15	15	15	15	10	10
Poisson's ratio, ν	0.28	0.28	0.28	0.28	0.28	0.28
Friction angle, φ (°)	–	–	–	–	28	28
Cohesion (MPa)	–	–	–	–	0	0
Dilation angle, ψ (°)	5	–	5	5	5	5

Table 2
The mineral composition and volume fractions at the initial stage are utilized for conducting reactive transport simulations in TOUGH-ECO_2N.

Mineral	Volume fraction	Reactive surface area (cm^2/g)
Primary mineral)		
Calcite	0.03	9.8
Quartz	0.475	9.8
Oligoclase	0.28	9.8
K-feldspar	0.2	9.8
Annite	0.0075	9.8
Muscovite	0.0075	151.6
Secondary mineral)		
Kaolinite	0.0	151.6
Smectite-Na	0.0	151.6
Chlorite	0.0	151.6
Illite	0.0	151.6
Hematite	0.0	12.9
Smectite-Ca	0.0	151.6
Albite	0.0	9.8
Dolomite	0.0	9.8
Siderite	0.0	9.8

Table 3
Initial total concentrations for primary chemical species (Gan et al., 2021).

Chemical species	Initial concentration (mol/kg)
H^+	4.32×10^{-3}
Na^+	9.9×10^{-2}
K^+	5.98×10^{-3}
Ca^{2+}	4.74×10^{-3}
Mg^{2+}	2.67×10^{-5}
HCO^{3-}	4.56×10^{-2}
Cl^-	1.001
SiO2(aq)	1.03×10^{-3}
Fe^{2+}	3.02×10^{-7}
SO_4^{2-}	1.32×10^{-9}
AlO^{2-}	1.36×10^{-8}

4.2. Dissolution and precipitation of minerals

The mineral's dissolution-precipitation response is predominantly elucidated using the Arrhenius equation, as denoted by Equation (7). We track the dissolution and precipitation of minerals. These include calcite, oligoclase and smectite, along with numerous others whose dissolution and precipitation reactions in faults will be detailed in the discussion section.

(1) Calcite dissolution

The dissolved CO_2 results in the rapid dissolution of calcite. The reactive interactions are as,

$$CaCO_3(solid) + CO_2 + H_2O \rightarrow Ca^{2+} + 2HCO_3^- \quad (23)$$

$$Ca^{2+} + 2HCO_3^- \rightarrow CaCO_3 + CO_2 + H_2O \quad (24)$$

The volume fraction of calcite changes over 1y-7y as depicted in Fig. 3. Due to the apparent increase in the concentration of H^+ over the preceding 1y-7y, calcite dissolution increases significantly. Nonetheless, under anhydrous conditions, the presence of high concentrations of $scCO_2$ near the injector restricts the dissolution of calcite that therefore excludes brine. Consequently, a small amount of calcite is precipitated at 900 m near the injector at 7y, consistent with equation (24). The continuous dissolution of calcite substantially raises the Ca^{2+} concentration in the reservoir and fault, but the low permeability of the fault core experiences little change in calcite to the right of the fault zone (outside the fault-bounded compartment), because the fault core restricts the diffusion of CO_2 and the pH value in this zone changes little.

(2) Oligoclase dissolution and smectite precipitation

Fig. 4 (a) illustrates a discernible dissolution of oligoclase through the observed change in its volume fraction at the 7y. Similar to calcite, its dissolution experiences inhibition near the injector due to the exclusion of the aqueous brine in its vicinity. Oligoclase dissolves preferentially under conditions of low pH, as demonstrated by equation (25):

$$CaNa_4Al_6Si_{14}(oligoclase) + 6H^+ + 19H_2O \leftrightarrow Ca^{2+} + 4Na^+ + 3Al_2Si_2O_5(OH)_4 + 8Si(OH)_4 \quad (25)$$

Consequently, the dissolution of oligoclase releases Ca^{2+} and Na^+, and promoting the subsequent precipitation of smectite (Fig. 4(b)). Fig. 5 presents the variations in volume fraction of oligoclase, smectite, Mg^{2+} and Na^+ within the reservoir and fault. From this, smectite precipitation ceases after 3y in the reservoir since the primary period of consumption of oligoclase by dissolution is at 1y-3y (Fig. 5 (a)). The acid pH condition on the fault causes the continuous dissolution of oligoclase at 3y-7y, resulting in the precipitation of smectite over the same period (Fig. 5 (b)).And the gradual increase in the volume fraction of Na^+ near the injector and the fault can be observed over the durations 1y-3y and 3y-7y, respectively, attribute to the dissolution of oligoclase. A consistent decline in the volume fraction of Mg^{2+} is evident in both the reservoir and the fault. This diminishing trend can be ascribed to its active involvement in the generation of Na-smectite and Ca-smectite, as indicated by equations (26) and (27). However, the incremental modification in the volume fraction of smectite precipitation remains marginal in both the reservoir and the fault, at 1.0×10^{-6} and 4.0×10^{-7} respectively, which has a negligible effect in changing porosity and permeability.

$$(Na-smectite)0.26Mg^{2+} + 0.29Na^+ + 1.77Al(OH)_3 + 3.97H_4SiO_4 \rightarrow Na_{0.24}Mg_{0.26}Al_{1.77}Si_{3.97}O_{10}(OH)_2 + 0.81H^+ + 9.19H_2O \quad (26)$$

$$(Ca-smectite)0.26Mg^{2+} + 0.145Ca^{2+} + 1.77Al(OH)_3 + 3.97H_4SiO_4 \rightarrow Ca_{0.145}Mg_{0.26}Al_{1.77}Si_{3.97}O_{10}(OH)_2 + 0.81H^+ + 9.19H_2O \quad (27)$$

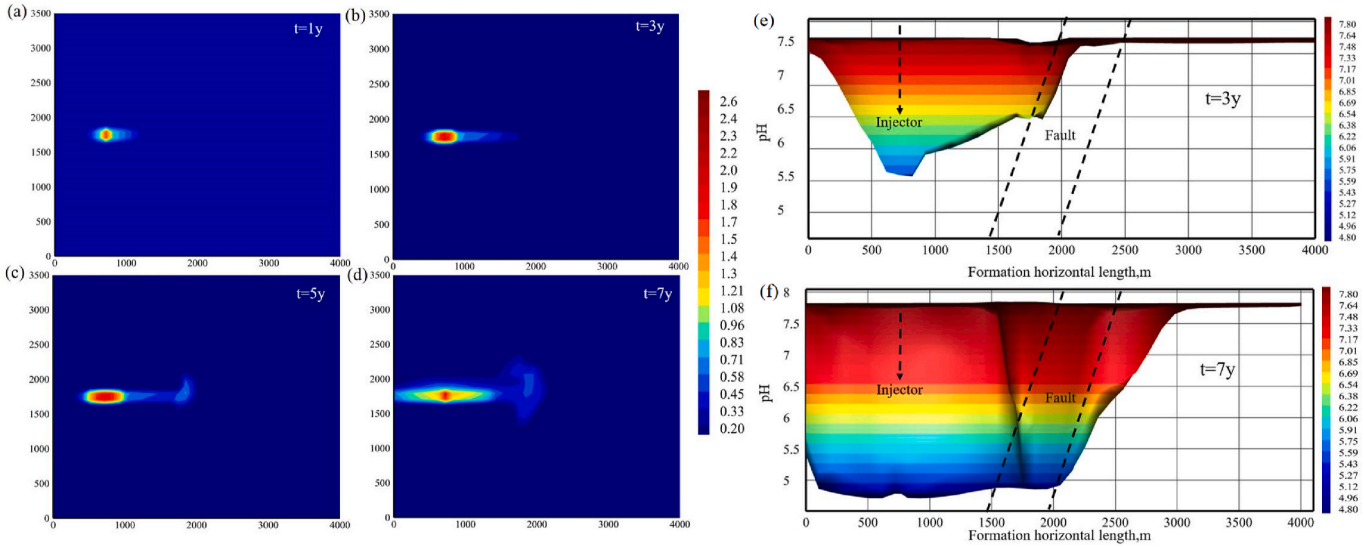

Fig. 2. Distribution of aqueous CO_2 concentration in mol/kg H_2O from 1y to7y (a–d), and distribution of pH value at (e) 3y, (f) 7y.

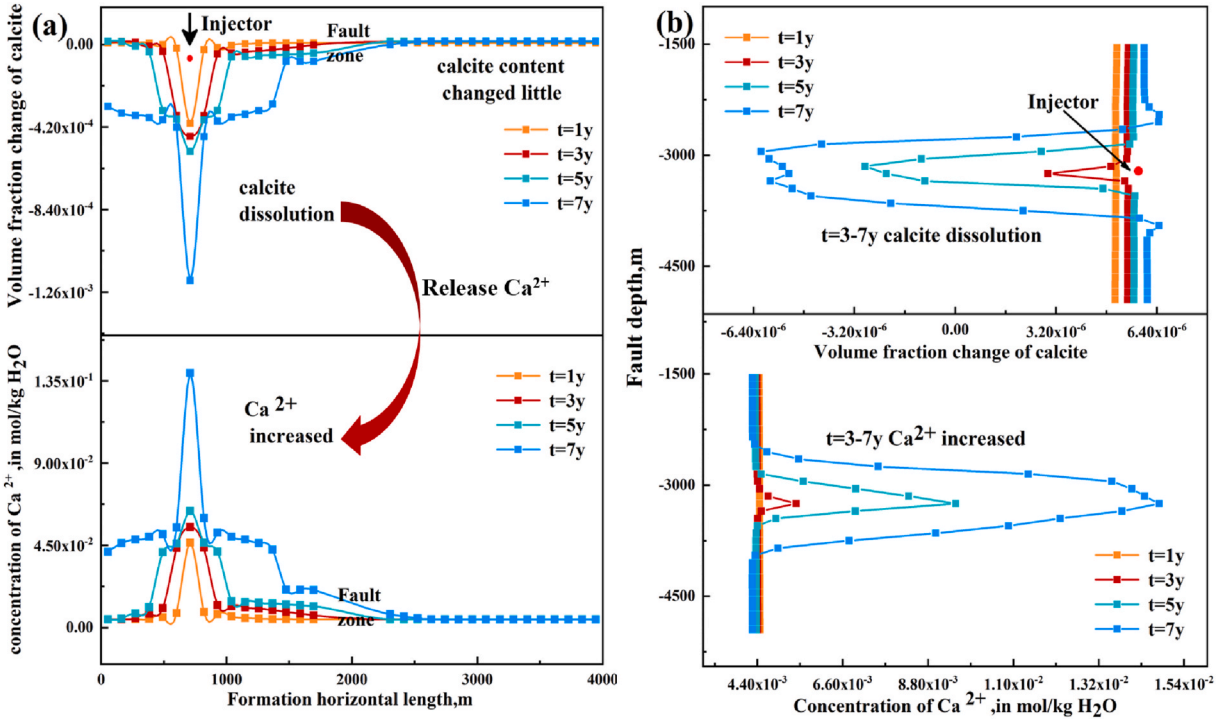

Fig. 3. Distribution of change in volume fraction of calcite and Ca^{2+} concentrations in (a) reservoir, and (b) fault from 1y to 7y.

5. Discussion

5.1. Fault stability analysis

Given the significant infiltration of aqueous CO_2 into the mid-height of the fault (Fig. 2 (f)), a plausible inference can be drawn that the fault experienced slip before 7y. Therefore, it is imperative to examine the stability of the fault during the 1y -5y. Fig. 6 (a) elucidates the dynamic behavior of pore pressure within the fault zone at 5y. It offers valuable insights into the intricate fluid dynamics governed by the fault core's low-permeability character. The fault core acts as a formidable impediment to fluid flow, inducing a substantial reduction in the flow rate across the fault plane. As a result, the accumulation of pressure on the right side of the damage zone is effectively alleviated, leading to a negligible flux. Remarkably, the pore pressure within the fault zone reaches a noteworthy magnitude of 52 MPa precisely at 5y.

Fig. 6 (b) presents the alterations in effective stress and shear stress within the fault. The gradual decline in effective stress can be attributed to the rising pore pressure, while the variations in total stress induce significant modifications in the spatial distribution of shear stress surrounding the fault. By comparing the Coulomb stress ratio (equation. (21)) to the friction coefficient, the activation time of the fault can be determined based on the two-dimensional stress analysis on the fault plane (Gan and Lei, 2020). Fig. 6 (b) also depicts the temporal evolution of the Coulomb stress ratio at specific monitoring points (J, R) along the fault zone, serving as a crucial tool for assessing the timing of fault activation. The Coulomb stress ratios at monitoring points J and R increase gradually then drop sharply as the fault reactivates at 6y (t = 1.9

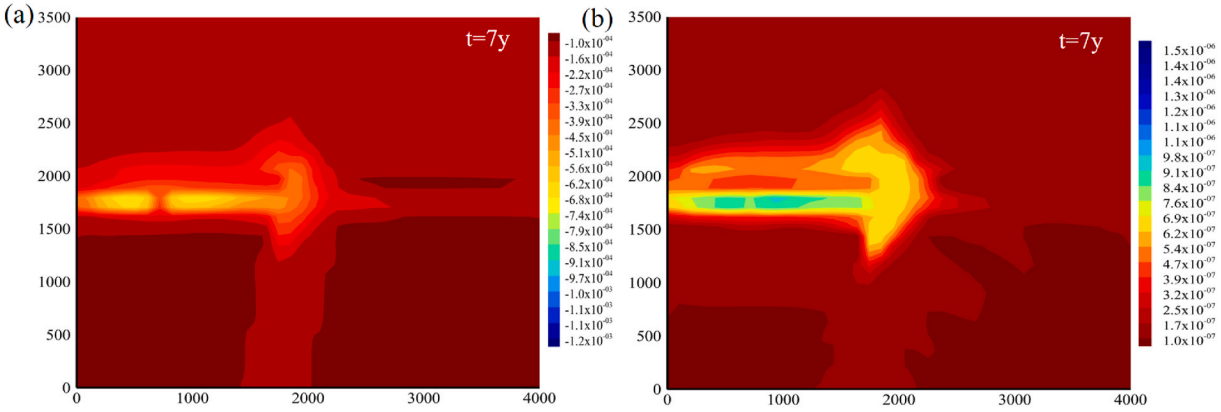

Fig. 4. Temporal evolution of (a) oligoclase (b) smectite volume fraction at 7y.

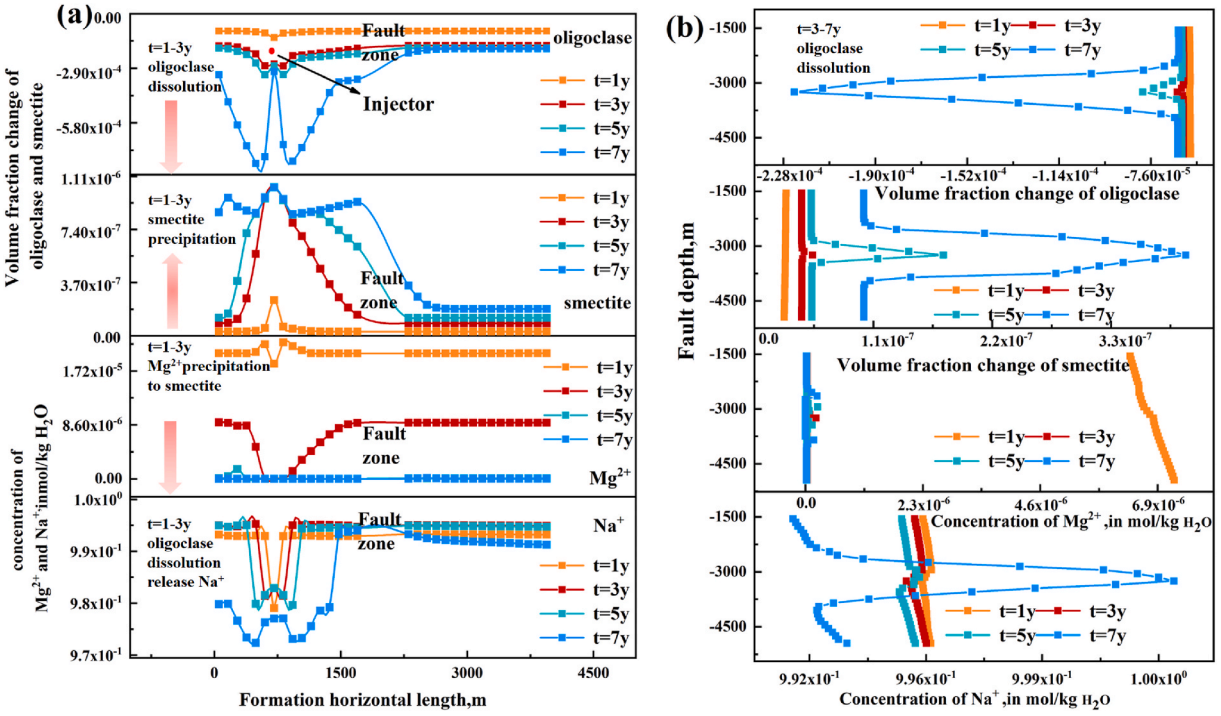

Fig. 5. Temporal evolution of oligoclase, smectite, Mg^{2+} and Na^{+} volume fraction in (a) reservoir, and (b) fault from 1y to 7y.

$\times$ 10^8 s). Fault slip is accompanied by CO_2 leakage with Fig. 6 (c) comparing the change in CO_2 saturation in the fault at 1y-7y. This shows that the permeable channel allows less CO_2 to enter the fault before slip is triggered (1y-5y), but reactivation promotes excessive CO_2 leakage beginning at 7y, increasing CO_2 saturation six-fold in the brine relative to that before sliding (i.e. at 5y).

5.2. Porosity & permeability evolution and fault self-sealing analysis

The behavior of reservoirs, particularly faults, can be characterized by their tendency to either undergo"self-sealing" through mineral precipitation or "self-enhancing" through mineral dissolution. This propensity is determined by the direction (decrease or increase) and rates at which porosity changes occur. Thus, the variations in porosity within the fault's damage zone and the fault itself can be utilized to assess the'rate of self-sealing' exhibited by the fault as (Caine et al., 1996; Patil and Mcpherson, 2020),

$$F_s = \frac{\left[\frac{(\phi_0-\phi)}{\phi_0}\right]*100}{t} \tag{28}$$

The initial porosity of the fault, labeled as ϕ_0, establishes a baseline. Over time, denoted as t years, the fault's porosity, represented as ϕ, undergoes change. The rate of fault self-sealing, F_s, measures the annual percentage shift in porosity. Positive values of F_s indicate self-sealing behavior, whereas negative values indicate porosity self-enhancing behavior.

Fig. 7 presents a comparison of the variation in volume fraction for minerals within the fault zone over a period of 5y, 6y, and 7y. It shows that the massive increase in leakage of CO_2 extends the range of reacting minerals at mid-height on the fault from ~2900 to 3500m to ~2400–4000m, corresponding to the acidic pH range along the fault (Fig. 9 (a)). In particular, oligoclase, calcite, and annite are the major minerals dissolved before the fault reactivates, while the remaining minerals (quartz, muscovite, illite, kaolinite, smectite and albite) are mainly precipitatied. After fault reactivation, oligoclase and annite

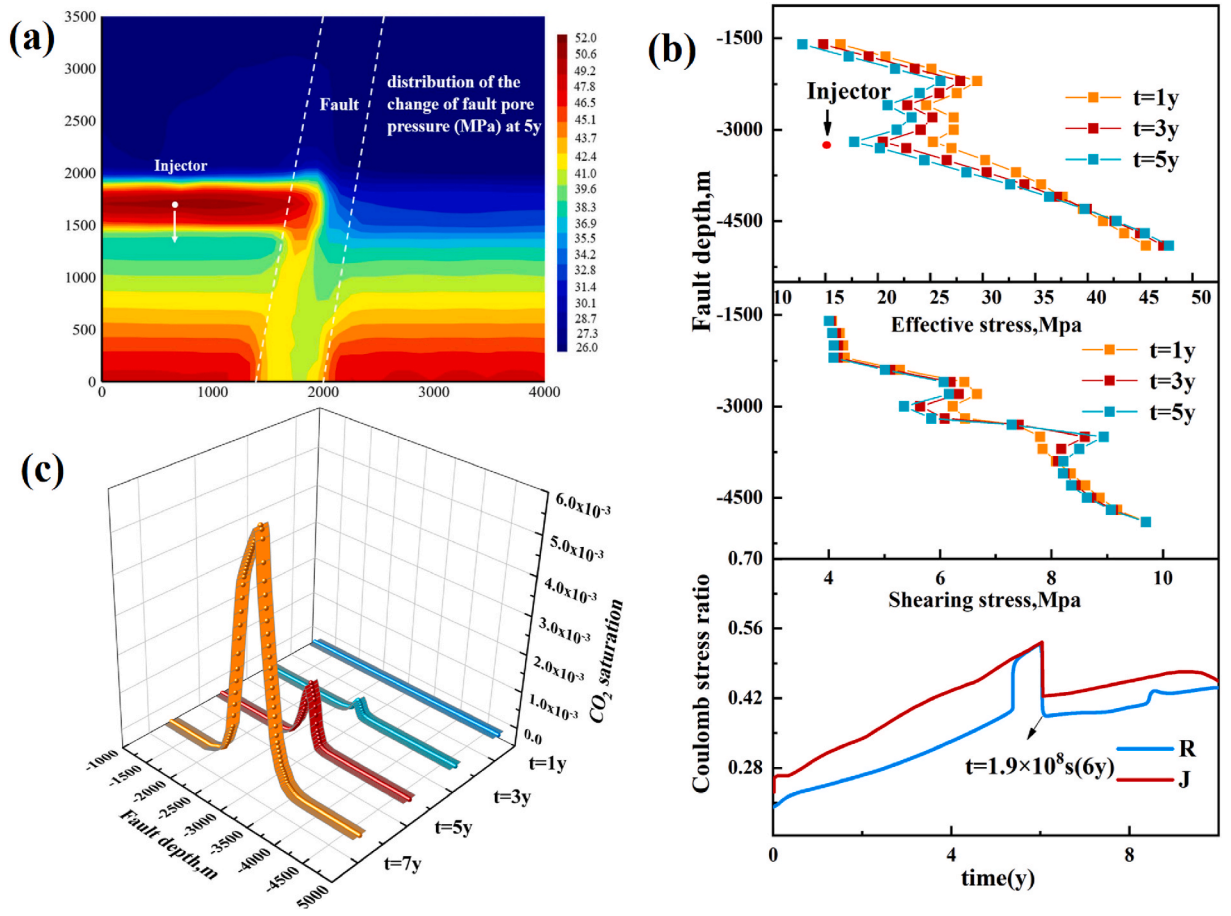

Fig. 6. Distribution of change in fault (a) pore pressure (MPa) at 5y, (b) effective stress and shear stress from 1y to 5y, evolution of Coulomb stress ratio at monitoring points (J, R) from 1y to 7y, (c) distribution of CO_2 saturation from 1y to 7y.

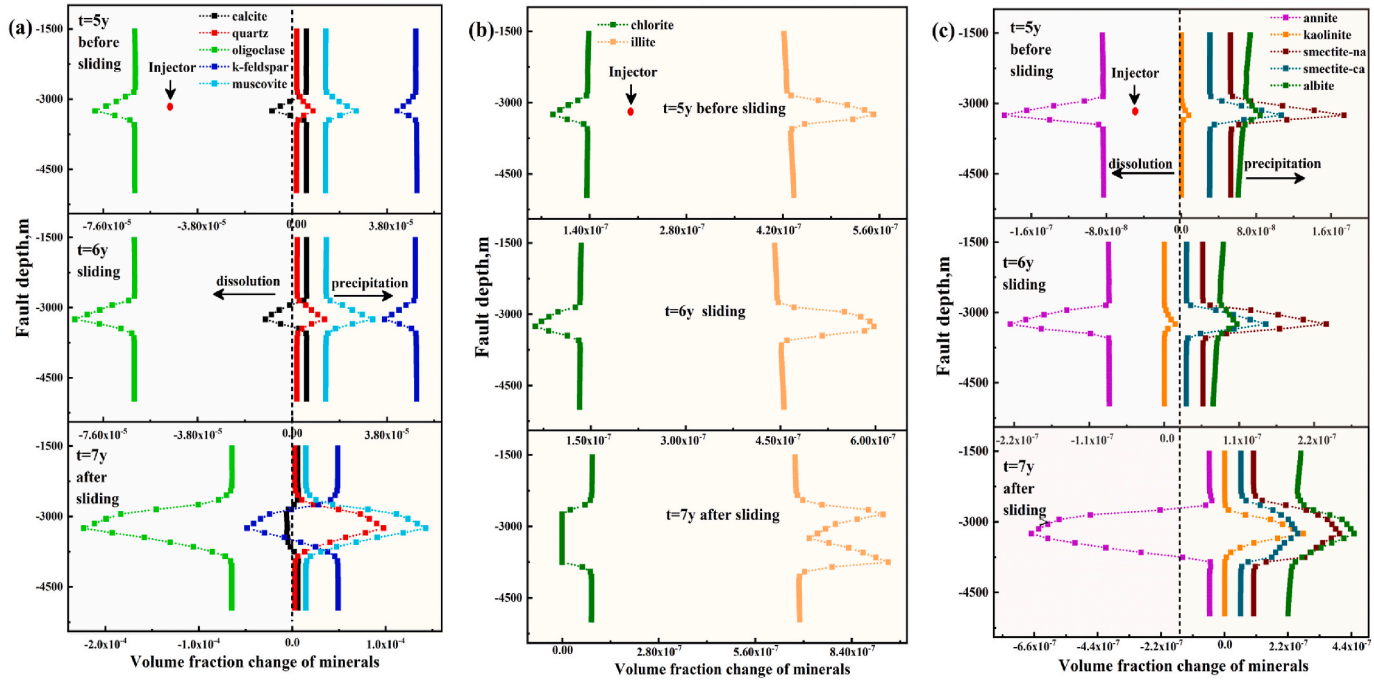

Fig. 7. Distribution of the change in mineral content within the fault at (a) 5y, (b) 6y, and (c) 7y.

dissolve substantially and the calcite remains unchanged. Most importantly, feldspar precipitation primarily occurs at 5y-6y, then the reactivation of the fault allows the penetration of CO_2 to dissolve the precipitated feldspar and its volume fraction decreases by ~80% at 7y. The dissolution of feldspar significantly boosts the formation of kaolinite, resulting in a tenfold increase in its volume fraction. The processes of mineral dissolution and precipitation are pivotal in modulating fault porosity, either by enhancing it or facilitating self-sealing. Feldspar dissolution notably amplifies porosity, while the subsequent kaolinite precipitation mitigates this increase, progressively aiding in the self-sealing of the fault zone.

The rich fluids CO_2 penetrates the entire middle-height of the fault, even though the fault core has low permeability after fault sliding (Fig. 8 (a)). Fig. 8(b) and (c) & (d) present the concentration distribution of mineral ions within the fault, focusing on the mid-height region. The concentration profiles were obtained by analyzing the fault damage zone and fault core individually at specific points (points a, b, c). Primary minerals like oligoclase, calcite, and feldspar undergo dissolution, leads to elevated concentrations of Ca^{2+}, Na^{+} and K^{+}. Among them, K^{+} exhibits the most significant increase, reaching approximately ten times higher concentration. This substantial rise in concentration is attributed to CO_2 leakage at 7y, which triggers the dissolution of a greater amount of feldspar compared to the 5y. And the precipitation of feldspar could significantly reduce the initial concentration of K^{+} from 5.98×10^{-3} to 5.23×10^{-5} at 5y (before fault reactivation), by about two orders of magnitude less.

Concurrently, fault activation leads to a substantial increase in fault porosity and permeability. In Fig. 9 (b), over the span of 0y to 7y, the changes in porosity and permeability within the fault are illustrated. Specifically, there is a 1.02 times increase in porosity and a 1.06 times increase in permeability, compared to their initial values after 7y of fault sliding, which clearly higher than over the first 5y-6y. Meanwhile, the migration of CO_2 from the deeper formation along the fault has minimal impact on the porosity and permeability at the fault base, specifically below the 4000m.

Moreover, we focus on the distribution of F_S along the fault to examine the breach in the local fault sealing response (Fig. 9 (b)). The Fs is positive at depths below −4500m, indicating self-sealing behavior, while negative values of Fs above −4500m indicate self-enhancing behavior before fault reactivation (5y-6y), with the entire fault presenting self-enhancing behavior after reactivation. This result indicates that the fault tends towards self-enhancing behavior with the increase of porosity and permeabil1ity. An important observation is that changes in mineral aqueous concentration in the fault zone can be used as indices to evaluate fault stability and as a diagnostic to distinguish between self-sealing and self-enhancing behavior. The fault is about to reactivate and the fault base (below −4500m) tends towards self-enhancing behavior when the initial aqueous concentration of K^{+} decreases significantly by two orders of magnitude.

It is paramount to investigate the impact of chemical fields, particularly mineral dissolution and precipitation, on fault porosity and permeability. Consequently, two parametric simulations are undertaken to examine the consequences of porosity and permeability evolution in different coupled and injection model scenarios. In the initial scenario (case 1), the fully coupled THMC model is demonstrated, which encompasses all interrelated processes. In contrast, Case 2 decouples the chemical influence and concentrates exclusively on the interaction between thermal, hydrological, and mechanical processes (T-H-M). By comparing these two cases, the effects of the chemical processes on porosity and permeability evolution can be analyzed. Founding that without the involvement of chemical fields (case 2), the porosity and permeability of the fault above −3000 m is slightly increased by about 0.03 times, while there is no change below −3000 m (Fig. 10(a) and (b)). Subtle changes unveil the influence of mineral dissolution and

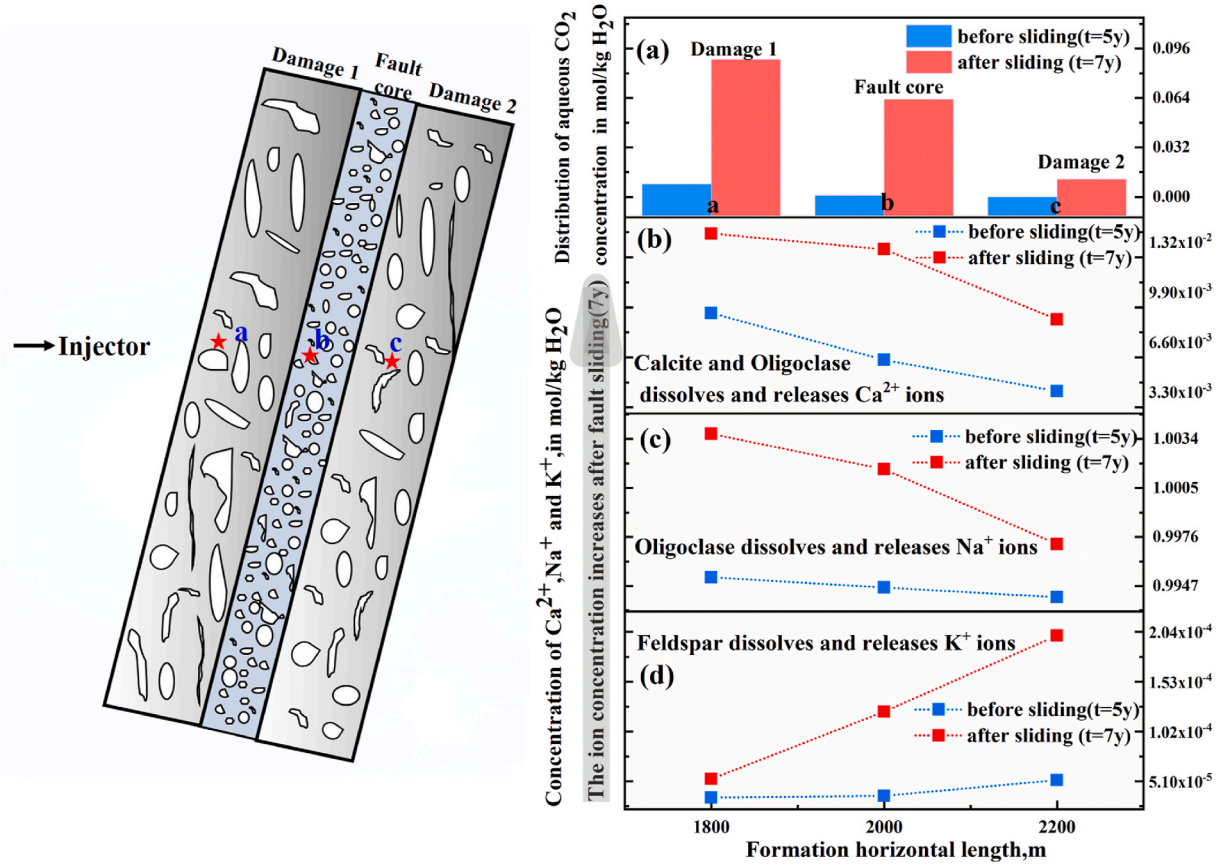

Fig. 8. Monitoring of CO_2 concentration and mineral ion concentration before and then after fault slip.

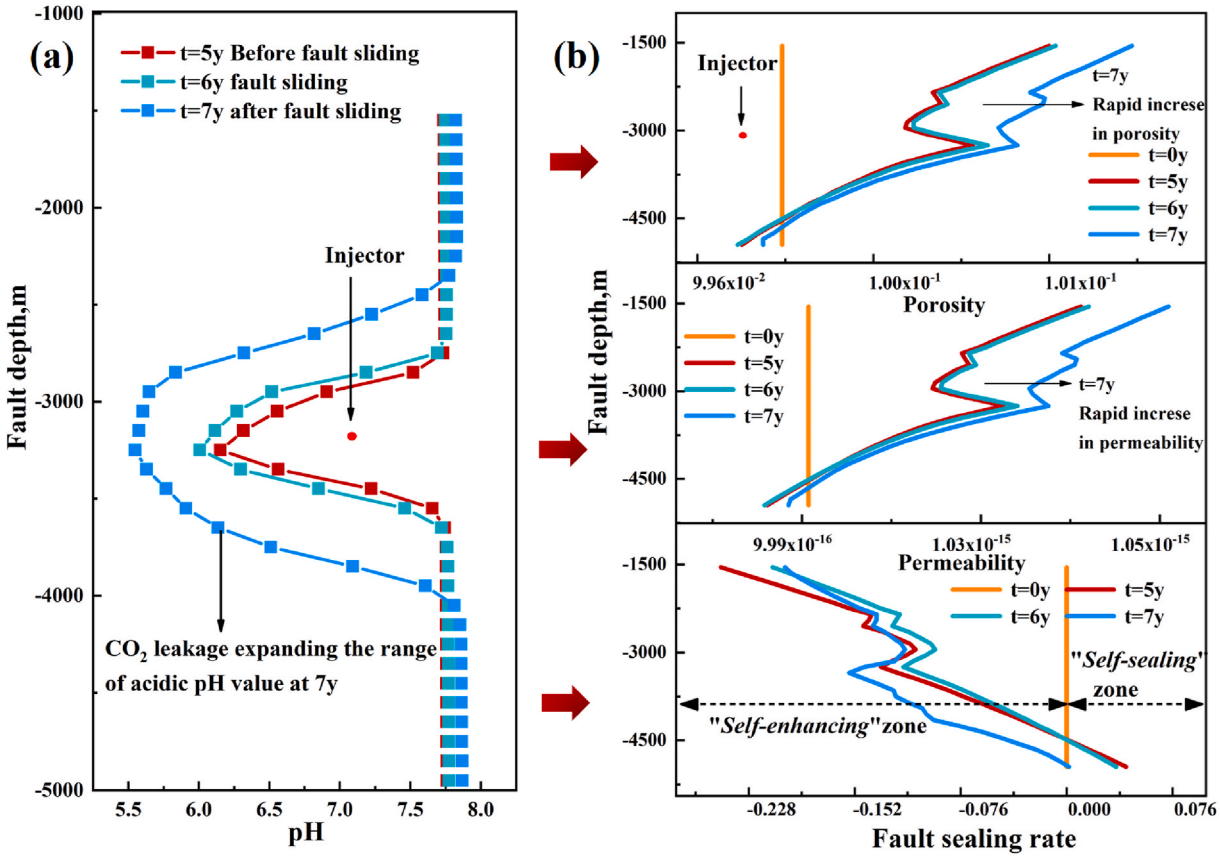

Fig. 9. Distribution of the change in (a) pH, (b) porosity, permeability (m^2), and fault sealing rate in the fault from 5y to 7y.

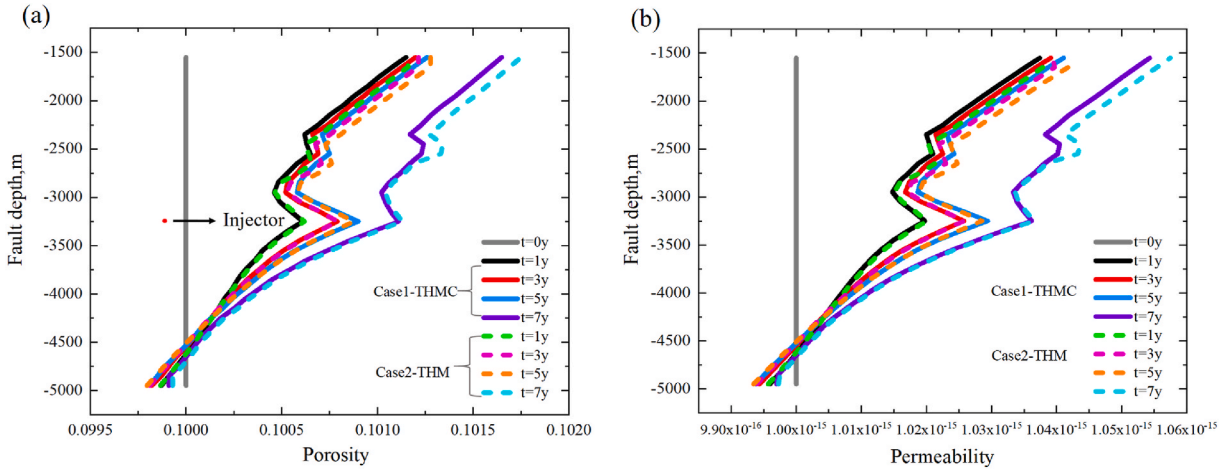

Fig. 10. Distribution of (a) porosity, and (b) permeability (m^2) in the fault from 1y to 7y at two simulation scenarios (Case 1–2).

precipitation on fault porosity and permeability. Particularly, within case 1, chemical reactions involving minerals assume a pivotal role in diminishing the porosity and permeability of the fault's middle and upper sections. This underscores the importance of mineral-related processes in shaping the structural properties of faults.

6. Conclusions

In this article, a comprehensive and fully-coupled methodology is presented for analyzing the effect of CO_2 injection on triggering fault instability. In contrast to conventional induced fault analysis, the resultant evolution of mineral concentration is also analyzed to determine the effect of reactive transport across the fault, mainly due to the disruption of fault transverse connectivity caused by reactivation. In this work, the rapid dissolution of calcite causes HCO_3^- increases greatly and reduces the pH in the formation after $scCO_2$ enters a reservoir. As pore pressure within the fault rises, the effective stress decreases accordingly, leading to the fault's activation at $t = 1.9 \times 10^8$s (6y). Permeability enhancement followed by the fault instability promotes excessive CO_2 leakage crossing fault rupture, and its CO_2 saturation inside fault is enhanced six-fold.

The evolution of the mineral kinetic precipitation/dissolution evolved the formation's porosity and permeability, especially after fault reactivated, which allows excessive CO_2 leakage transport across fault.

The shear failure following CO_2 leakage cause the feldspar and oligoclase to dissolve, and secondary clay minerals precipitate, which makes the porosity and permeability of fault zone increase by only 2% and 6% respectively. Comparison of mineral concentrations adjacent to the fault before-and-after instability revealed that the development of shear failure actually also promotes the transport of reactivate minerals into fault zones. The fault reactivation causes dissolution reaction dominated by feldspar at its later stage, with the volume fraction decreases by 80%. The transport of minerals changes the fault porosity and permeability further affect its self-sealing behavior in the bottom of fault, while the top of fault presents a self-enhancing response. The change of the concentration of K^+ before fault reactivation in fault zone can be used as indexes to characterize fault stability and self-sealing response. The different simulation scenarios indicate that the chemical reactions of minerals could slightly decrease the middle and upper part of fault porosity and permeability.

The study offers valuable insights into the self-sealing and self-enhancing behaviors of faults, emphasizing the impact of mineral dissolution and precipitation on CO_2 leakage, while also introducing a novel method for monitoring fault behavior in carbon storage projects by identifying changes in mineral ion concentrations as indicators of fault stability and the progress of self-sealing behavior.

CRediT authorship contribution statement

Lian Chen: Writing – review & editing, Writing – original draft, Conceptualization. **Derek Elsworth:** Supervision, Software, Formal analysis. **Jianye Chen:** Supervision. **Quan Gan:** Writing – review & editing, Supervision, Software.

Declaration of competing interest

All authors disclosed no relevant relationships.

Acknowledgments

This study received financial support from the China National Key Research and Development Program (Grant: 2021YFC3000603), the Natural Science Foundation of China (Grant No. 52174165 and 5217041034), CO_2 Enhanced Shale Gas Recovery and Sequestration by Numerical Thermal-Hydro-Mechanical-Chemical Modeling (Grant: 2022DQ020206), and the Science and Technology Department of Sichuan Province (Grant: 22SYSX0052).

Data availability

The data sharing link has been added at the end of the article

References

Alexey, Y., Konstantin, T., Sinem, Y., Pavel, S., Roman, I., Evgenii, S., 2022. Seismic monitoring of CO_2 geosequestration using multi-well 4D DAS VSP: stage 3 of the CO_2 CRC otway project. Int. J. Greenh. Gas Control 119. https://doi.org/10.1016/J.IJGGC.2022.103726.

Andersen, O.A., Nilsen, H.M., Gasda, S.E., 2017. Vertical equilibrium flow models with fully coupled geomechanics for CO_2 storage modeling, using precomputed mechanical response functions. Energy Proc. 114, 3113–3131. https://doi.org/10.1016/j.egypro.2017.03.1440.

Andreani, M., Gouze, P., Luquot, L., Jouanna, P., 2008. Changes in seal capacity of fractured claystone caprocks induced by dissolved and gaseous CO_2 seepage. Geophysical Reserch Letters 35 (14), 1–6. https://doi.org/10.1029/2008GL034467.

Caine, S.J., Evans, P.J., Forster, B.C., 1996. Fault zone architecture and permeability structure. Geology 24 (11), 1025–1028. https://doi.org/10.1130/0091-7613(1996)024<1025:FZAAPS>2.3.CO;2.

Caulk, R.A., Ghazanfari, E., Perdrial, N.J., Perdrial, N., 2016. Experimental investigation of fracture aperture and permeability change within enhanced geothermal systems. Geothermics 62 (7), 12–21. https://doi.org/10.1016/j.geothermics.2016.02.003.

Cerasi, P., Stroisz, A., Sønstebø, E., Stanchits, S., Oye, V., Bauer, R., 2018. Experimental investigation of injection pressure effects on Fault Reactivation for CO_2 storage. Int. J. Greenh. Gas Control 78, 218–227. https://doi.org/10.1016/j.ijggc.2018.08.011.

Davies, J.P., Davies, D.K., 2001. Stress-dependent permeability: characterization and modeling. Society of Petroleum Engineers 6 (2), 224–235. https://doi.org/10.2118/71750-PA.

Ellsworth, William, L., 2013. Injection-induced earthquakes. Science 341 (6142). https://doi.org/10.1126/science.1225942.

Espinoza, D.N., Jung, H., Major, J.R., Sun, Z., Ramos, M.J., Eichhubl, P., 2018. CO_2 charged brines changed rock strength and stiffness at crystal geyser, Utah: implications for leaking subsurface CO_2 storage reservoirs. Int. J. Greenh. Gas Control 73, 16–28. https://doi.org/10.1016/j.ijggc.2018.03.017.

Falcon-Suarez, I., Canal-Vila, J., Delgado-Martin, J., North, L., Best, A., 2017. Characterisation and multifaceted anisotropy assessment of corvio sandstone for geological CO_2 storage studies. Geophys. Prospect. 65 (5), 1293–1311. https://doi.org/10.1111/1365-2478.12469.

Gan, Q., Elsworth, D., 2014a. Thermal drawdown and late-seismic slip Fault Reactivation in enhanced geothermal reservoirs. J. Geophys. Res. Solid Earth 119 (12), 8936–8949. https://doi.org/10.1002/2014JB011323.

Gan, Q., Elsworth, D., 2014b. Analysis of fluid injection-induced Fault Reactivation and seismic slip in geothermal reservoirs. J. Geophys. Res. Solid Earth 119 (4), 3340–3353. https://doi.org/10.1002/2013JB010679.

Gan, Q., Lei, Q.H., 2020. Induced Fault reactivation by thermal perturbation in enhanced geothermal systems. Geothermics 86 (C), 101814. https://doi.org/10.1016/j.geothermics.2020.101814, 101814.

Gan, Q., Elsworth, D., Alpern, J.S., Marone, C., Connolly, P., 2015. Breakdown pressures due to infiltration and exclusion in finite length boreholes. J. Pet. Sci. Eng. 127, 329–337. https://doi.org/10.1016/j.petrol.2015.01.011.

Gan, Q., Candela, T., Wassing, B., Wasch, L., Liu, J., Elsworth, D., 2021. The use of supercritical CO_2 in deep geothermal reservoirs as a working fluid: insights from coupled THMC modeling. Int. J. Rock Mech. Min. Sci. 147. https://doi.org/10.1016/J.IJRMMS.2021.104872.

González-Nicolás, A., Cihan, A., Petrusak, R., Zhou, Q.L., Trautz, R., Riestenberg, D., 2019. Pressure management via brine extraction in geological CO_2 storage: adaptive optimization strategies under poorly characterized reservoir conditions. Int. J. Greenh. Gas Control 83, 176–185. https://doi.org/10.1016/j.ijggc.2019.02.009.

Guglielmi, Y., Birkholzer, J., Rutqvist, J., Jeanne, P., Nussbaum, C., 2017. Can Fault leakage occur before or without reactivation? Results from an in situ Fault Reactivation experiment at mont terri. Energy Proc. 114, 3167–3174. https://doi.org/10.1016/j.egypro.2017.03.1445.

Jaeger, J.C., Cook, N., 1979. Fundamentals of rock mechanics. Science Paperbacks 9 (3), 251–252. https://doi.org/10.1111/j.1468-8123.2009.00251.x third edition.

Lang, P.S., Paluszny, A., Zimmerman, R.W., 2015. Hydraulicsealing due to pressure solution contact zone growth in silici-clastic rock fractures. J. Geophys. Res. Solid Earth 120 (6), 4080–4101. https://doi.org/10.1002/2015JB011968.

Lasaga, A.C., 1984. Chemical kinetics of water-rock interactions. J. Geophys. Res. 89, 4009–4025.

Li, Z.Q., Ma, X.D., Kong, X.Z., Saar, M.O., Vogler, D., 2020. Permeability evolution during pressure-controlled shear slip in saw-cut and natural granite fractures. Rock Mechanics Bulletin 2 (2), 100027. https://doi.org/10.1002/essoar.10505296.1.

Li, Z., Lv, Y.F., Liu, B., 2022. Numerical simulation of CO_2 migration and geochemical reactions in shihezi formation caprock, China. Energies 16 (1), 92. https://doi.org/10.3390/EN16010092, 92.

Ma, D., Rezania, M., Yu, H.S., Bai, H.B., 2017. Variations of hydraulic properties of granular sandstones during water inrush: effect of small particle migration. Eng. Geol. 217, 61–70. https://doi.org/10.1016/j.enggeo.2016.12.006.

Ma, Y.Q., Xia, K.W., Lei, Q.H., Zhang, C.Y., Yuan, L., 2024. Roles of heat and stress transfer in triggering fault instability in conjugate faulted reservoirs. Int. J. Rock Mech. Min. Sci. 180, 105819, 105819.

McDermott, C., Bond, A., Harris, F.A., Chittenden, N., Thatcher, K., 2015. Application of hybrid numerical and analytical solutions for the simulation of coupled thermal, hydraulic, mechanical and chemical processes during fluid flow through a fractured rock. Environ. Earth Sci. 74 (12), 7837–7854. https://doi.org/10.1007/s12665-015-4769-9.

Minh, T., Birendra, J., 2021. Effect of poroelastic coupling and fracture dynamics on solute transport and geomechanical stability. Water Resour. Res. 57 (10). https://doi.org/10.1029/2021WR029584.

Nicol, A., Carne, R., Gerstenberger, M., Christophersen, A., 2011. Induced seismicity and its implications for CO_2 storage risk. Energy Proc. 4, 3699–3706. https://doi.org/10.1016/j.egypro.2011.02.302.

Ogata, S., Yasuhara, H., Kinoshita, N., Cheon, D.S., Kishida, K., 2018. Modeling of coupled thermal-hydraulic-mechan-ical-chemical processes for predicting the evolution in permeability and reactive transport behavior within single rock fractures. Int. J. Rock Mech. Min. Sci. 107, 271–281. https://doi.org/10.1016/j.ijrmms.2018.04.015.

Palandri, J., Kharaka, Y.K., 2004. A compilation of rate parameters of water-mineral interaction kinetics for application to geochemical modeling. US Geol. Surv. Open File Report 2004-1068 64.

Patil, V.V., Mcpherson, B.J., 2020. Identifying hydrogeochemical conditions for fault self-sealing in geological CO_2 storage. Water Resour. Res. 56 (3). https://doi.org/10.1029/2018WR024436.

Patil, V.V., McPherson, B.J., Priewisch, A., Moore, J., Moodie, N., 2017. Factors affecting self-sealing of geological faults due to CO_2-leakage. Greenhouse Gases: Sci. Technol. 7 (2), 273–294. https://doi.org/10.1002/ghg.1673.

Perera, M.S.A., Rathnaweera, T.D., Ranjith, P.G., Wanniarachchi, W.A.M., Haque, A., 2016. Laboratory measurement of deformation-induced hydro-mechanical properties of reservoir rock in deep saline aquifers: an experimental study of hawkesbury formation. Mar. Petrol. Geol. 77, 640–652. https://doi.org/10.1016/j.marpetgeo.2016.07.012.

Peter, C., Lichtner, 1996. Continuum formulation of multicomponent-multiphase reactive transport. Rev. Mineral. Geochem. 34 (1), 1–81.
Pruess, K., 2004. The TOUGH codes—a family of simulation tools for multiphase flow and transport processes in permeable media. Vadose Zone J. 3 (3), 738–746. https://doi.org/10.2136/vzj2004.0738.
Pruess, K., Muller, N., 2009. Formation dry-out from CO_2 injection into saline aquifers: 1. Effects of solids precipitation and their mitigation. Water Resour. Res. 45 (3). https://doi.org/10.1029/2008wr007101.
Reddy, P.P., Balaji, K., Kumar, V.S., 2022. Investigation of solubility trapping mechanism during geologic CO_2 sequestration in deccan volcanic provinces, Saurashtra, Gujarat, India. Int. J. Greenh. Gas Control 120. https://doi.org/10.1016/j.ijggc.2022.103769.
Rinaldi, A.P., Rutqvist, J., Finsterle, S., Liu, H.H., 2016. Inverse modeling of ground surface uplift and pressure with itough-pest and tough-flac: the case of CO_2 injection at in salah, Algeria. Comput. Geosci. 108, 98–109. https://doi.org/10.1016/j.cageo.2016.10.009.
Rohmer, J., Pluymakers, A., Renard, F., 2016. Mechano-chemical interactions in sedimentary rocks in the context of CO_2 storage: weak acid weak effects? Earth Sci. Rev. 157, 86–110. https://doi.org/10.1016/j.earscirev.2016.03.009.
Rutqvist, J., Wu, Y.S., Tsang, C.F., Bodvarsson, G., 2002. A modeling approach for analysis of coupled multiphase fluid flow, heat transfer, and deformation in fractured porous rock. Int. J. Rock Mech. Min. Sci. 39 (4), 429–442. https://doi.org/10.1016/S1365-1609(02)00022-9.
Saro, M., Birendra, J., 2021. Quantification of fault leakage dynamics based on leakage magnitude and dip angle. Int. J. Numer. Anal. Methods GeoMech. 45 (16), 2303–2320. https://doi.org/10.1002/NAG.3267.
Schwab, R.D., Bidgoli, S.T., Taylor, H.M., 2017. Characterizing the potential for injection-induced Fault Reactivation through subsurface structural mapping and stress field analysis, wellington field, sumner county, Kansas. J. Geophys. Res. Solid Earth 122 (12), 10132–10154. https://doi.org/10.1002/2017JB014071.
Shemeta, J.E., Eide, E.A., Hitzman, M.W., Clarke, D.D., Detournay, E., Dieterich, J.H., 2012. The potential for induced seismicity in energy technologies. Lead. Edge 31 (12), 1438–1444. https://doi.org/10.1190/tle31121438.1.
Shi, Q., Cui, S., Wang, S., Mi, Y., Sun, Q., Wang, S., 2022. Experiment study on CO_2 adsorption performance of thermal treated coal: inspirationfor CO_2 storage after underground coal thermal treatment. Energy 254 (PA). https://doi.org/10.1016/j.energy.2022.124392.
Snow, David, T., 1969. Anisotropic permeability of fractured media. Water Resour. Res. 5 (6), 1273–1289. https://doi.org/10.1029/wr005i006p01273.
Steefel, C.I., Lasaga, A.C., 1994. A coupled model for transport of multiple chemical species and kinetic precipitation/dissolution reactions with applications to reactive flow in single phase hydrothermal system. Am. J. Sci. 294, 529–592.
Suckale, J., 2010. Moderate-to-Large seismicity induced by hydrocarbon production. Lead. Edge 29 (3), 310–319. https://doi.org/10.1190/1.3353728.
Taghizadeh, R., Goshtasbi, K., Manshad, A.K., Ahangari, K., 2019. Geomechanical assessment of reservoir and caprock in CO_2 storage: a coupled THM imulation. Advances in Energy Research 6 (1), 75–90.
Taron, J., Elsworth, D., Min, K.B., 2009. Numerical simulation of thermal-hydrologic-mechanical-chemical processes in deformable, fractured porous media. Int. J. Rock Mech. Min. Sci. 46 (5), 842–854.
Valentina, Baranova, Azer, Mustaqeem, Sebastian, Bell, 1999. A model for induced seismicity caused by hydrocarbon production in the western Canada sedimentary basin. Can. J. Earth Sci. 36 (1), 47–64. https://doi.org/10.1139/e98-080.
Wang, X.L., Liu, H.H., Zhang, D.M., Yuan, X.Z., Zeng, P., Zhang, H., 2022. Effects of CO_2 adsorption on molecular structure characteristics of coal: implications for CO_2 geological sequestration. Fuel 321. https://doi.org/10.1016/j.fuel.2022.124155.
Wu, Y., Liu, j., Elsworth, D., Chen, Z., Connell, L., Pan, Z., 2010. Dual poroelastic response of a coal seam to CO_2 injection. Int. J. Greenh. Gas Control 4 (4), 668–678.
Yasuhara, H., Kinoshita, N., Ogata, S., Cheon, D.S., Kishida, K., 2016. Coupled thermo-hydro-mechanical-chemical modeling by incorporating pressure solution for estimating the evolution of rock permeability. Int. J. Rock Mech. Min. Sci. 86, 104–114. https://doi.org/10.1016/j.ijrmms.2016.03.015.
Yin, S., Dusseault, M.B., Rothenburg, L., 2011. Coupled THMC modeling of CO_2 injection by finite element methods. J. Petrol. Sci. Eng. 80 (1), 53–60. https://doi.org/10.1016/j.petrol.2011.10.O08.
Yoosook, H., Maneeintr, K., 2018. CO_2 geological storage coupled with water alternating gas for enhanced oil Recovery. Chemical Engineering Transactions 63. https://doi.org/10.3303/CET1863037.
Yu, Z.C., Liu, L., Yang, S.Y., Li, S., Yang, Y.Z., 2012. An experimental study of CO_2–brine–rock interaction at in situ pressure–temperature reservoir conditions. Chem. Geol. 326–327, 88–101. https://doi.org/10.1016/j.chemgeo.2012.07.030.
Zhang, R.L., Winterfeld, H.P., Yin, X.L., Xiong, Y., Wu, Y.S., 2015. Sequentially coupled THMC model for CO_2 geological sequestration into a 2D heterogeneous saline aquifer. J. Nat. Gas Sci. Eng. 27, 579–615. https://doi.org/10.1016/j.jngse.2015.09.013.
Zhang, Q., Ma, D., Wu, Y., Meng, F., 2018. Coupled thermal-gas-mechanical (TGM) model of tight sandstone gas wells. J. Geophys. Eng. 15 (4), 174–1752, 2018.
Zhang, Q., Ma, D., Liu, J., Wang, J., Li, X., Zhou, Z., 2019. Numerical simulations of fracture propagation in jointed shalereservoirs under CO_2 fracturing. Geofluids 2019.
Zhou, Z.L., Cai, X., Ma, D., Chen, L., Wang, S.F., Tan, L.H., 2018. Dynamic tensile properties of sandstone subjected to wetting and drying cycles. Construct. Build. Mater. 182 (10), 215–232. https://doi.org/10.1016/j.conbuildmat.2018.06.056.